All-in-One "Turn-on" Bionanoprobe for Self-Driving Immune Check-Point Blockage and Monitoring of the Spatiotemporal-Sensitive Immune Response in Acute Myeloid Leukemia

Dangui Zhang[a,b], Honglian Wu[c], Tianci Wang[a], Yuting Wang[a], Sixi Liu[a], ,Feiqiu Wen[a*],Gerile Oudeng[a*], Mo Yang [c*]

[a] Department of Hematology and Oncology, Shenzhen Children's Hospital of Shantou University Medical College, Futian, Shenzhen, Guangdong, 518026 PR China

[b] Research Center of Translational Medicine, Second Affiliated Hospital of Shantou University Medical College, Shantou, Guangdong, 515041 PR China

[c] Department of Biomedical Engineering, Hong Kong Polytechnic University, Hung Hom, Kowloon, 999077 Hong Kong SAR, PR China

ABSTRACT: Immune checkpoint (ICP) blocking (ICB) is one of the most promising immunotherapies for acute myeloid leukemia (AML). However, owing to their heterogeneity, AML cells may cause an uncoordinated metabolic flux and a heterogeneous immune response, inducing the spatiotemporal-sensitive process of immune response marker release. Precise and timely detection of immune response in ICB therapy is important for therapeutic strategy adjustment. Herein, we constructed an all-in-one nanoprobe for self-driving both the ICB and simultaneous immune response detection in the small AML cell *in vivo*. It enabled accurate evaluation of the heterogenetic immune response of living AML mice without additional drug treatment or probe processes. Dopamine hydrochloride-derived polydopamine (PDA) nanoparticles were loaded with an ICP blocker targeted to a new ICP (blocker of the immunity globulin-like receptor B4 receptor) of AML cells and induced the release of immune response marker granzyme B (GrB). Simultaneously, PDA nanoparticles were paired with the organic graphene quantum dots (GQD) to construct a "turn-on" fluorescence resonance energy transfer bionanoprobe for GrB detection. This multifunctional nanoprobe was validated to trigger ICB therapy and monitor the changes of GrB levels in real-time both at an intracellular level and in AML mice. The nanosized organic nanoprobe showed excellent permeability and retention in tumor cells and high biocompatibility *in vivo*. PDA nanoparticles with both excellent surface loading and optical quenching ability combined with excellent fluorescence properties of GQD offered the possibility of self-driven ICB therapy, with timely and non-invasive monitoring of the immune efficacy in an integrated system.

Acute myeloid leukemia (AML) is a group of hematological malignancies caused by the clonal proliferation of hematopoietic stem cells and has had a poor prognosis with increasing incidence worldwide over the last 30 years [1]. Presently, immunotherapy aims to reactivate the antileukemia immunity of patients and strengthen their immune function, thereby reducing reliance on intensive chemotherapy [2, 3]. Immune checkpoint (ICP) blocking (ICB) is an important immunotherapeutic approach for killing leukemia cells through cosuppressive or costimulatory signaling to modulate T-cell activity [4]. However, AML cells are highly heterogeneous; therefore, after several generations of division, their daughter cells may show considerably different immune drug sensitivity, resulting in differential cell proliferation and immune cell invasion. ICBs often cause stromal alternation, resulting in an uncoordinated metabolic flux and a heterogeneous immune response [3,5]. Hence, real-time monitoring of the immune response of patients with tumor post-ICB treatment is crucial for a precise and early evaluation of the therapy efficacy.

Currently, the therapy efficacy mainly depends on standard imaging technologies, such as positron emission tomography, computed tomography, and magnetic resonance imaging [6]. However, morphological imaging is limited to the monitoring of early responses at the molecular level. Additionally, immune responses are highly dependent on tumor microenvironment, which are nonreproducible ex vivo. Standard imaging techniques are generally an "always-on" system, which is limited to distinguishing the exhaustion and immunosuppression of T cells [7, 8]. Therefore, dynamic monitoring of immune response molecular markers *in vivo* is required for the early identification of responders and non-responders [9]. In response to ICB therapy, activated T cells interact with target tumor cells and induce apoptosis through granule exocytosis and the death ligand/death receptor system [5]. Granzyme B (GrB), a serine protease secreted by cytotoxic T lymphocytes (CTLs), plays a critical role in inducing tumor cell apoptosis [6,9]. Monitoring GrB activity could provide information regarding CTL performance and immune activation kinetics [7].

In ICB therapy, GrB-release-induced T cell activation in AML cells is a spatiotemporal sensitive process [8]. Especially in highly heterogeneous AML cell populations, it is crucial to synchronously deliver the ICP blocker and GrB probe to the AML cells to ensure the ICB therapy driving and GrB activity capturing within a specific time and space. Moreover, for patients with leukemia with incomplete immune function, frequent dosing, and traditional detection reagents or inorganic sensing materials are highly toxic. Organic bionanomaterials are emerging as potential candidates for use in ICB therapies owing to their extremely high biocompatibility. Among them, brain secretion-derived polydopamine (PDA) nanoparticles have the advantages of mild synthesis conditions,

feasibility for surface modification, good optical absorption, and degradability, which facilitates their important role in drug delivery and tumor photothermal therapy in recent years [9-12]. However, approaches to combine its nanoscale, surface, and optical features with other active biomolecules to achieve a more comprehensive capability on simultaneous tracking of therapy efficiency are unexplored.

Therefore, herein, an all-in-one bionanoprobe was constructed by using PDA nanoparticles as both an ICP block carrier and an optical quencher of the GrB sensing probe. The blocker of the immunity globulin-like receptor B4 (LILRB4), a newly discovered ICP for myeloid cells was conjugated on PDA to target the LILRB4-overexpressed AML cells and block its expression [13，14]. Then graphene quantum dots (GQDs) with red fluorescence was labeled on the GrB-cleavable peptide for tissue penetration. A fluorescence resonance energy transfer (FRET) bionanoprobe was constructed by pairing GQD (donor) and PDA (acceptor). This multifunctional bionanoprobe was investigated for self-driving of ICB therapy and real-time visualization of GrB levels both in vitro and *in vivo*. The detected GrB signal, T-cell infiltration, and the anti-tumor effect of humanized AML mice were systematically analyzed to evaluate this bionanoprobe.

EXPERIMENTAL SECTION

The details of materials, synthesis and characterizations are presented in the Supporting Information.

Preparation of BP-PDA bionanoprobe. PDA nanoparticles were prepared according to previously reported methods [11]. PDA dispersion was diluted to 2 mg mL^{-1} using water, and the pH was adjusted to 10 by adding NaOH (1M). NH_2-PEG-COOH was then added to the solution and stirred for 12 h at 25°C. The mass ratio of NH_2-PEG-COOH to PDA was 5:1. Then, the PEGylated PDA nanoparticles (PDA–PEG) were purified by ultrafiltration (molecular weight cut-off: 100 KDa) three times and stored at 4°C for future use. Next, the LILRB4 monoclonal antibody (mAb) was conjugated to PDA–PEG through EDC/NHS chemistry. Briefly, the EDC/NHS solution was freshly prepared (molar ratio of 2:1) and mixed with PDA–PEG to activate its carboxyl group. Then, LILRB4 mAb was added and the solution was stirred for 12 h at 4°C to obtain the mAb blocker-modified PDA nanocomposites (denoted as B-PDA). Excess mAb was removed by a centrifugation at 12000 rpm for 10 min.

GQD was mixed with EDC at a molar ratio of 1:3000 for 30 min at room temperature to activate the carboxyl groups of GQD. The GrB-recognized peptides (GK–IEPD–APC) with free amino groups (1 mg) were first uniformly dispersed and then added to the GQDs dispersion and stirred for 5 h at a low speed. After the reaction, the mixture was centrifuged at 8000 rpm for 3 min to remove the agglomerated precipitates. Then the collected sample in the supernatant was concentrated and purified by ultrafiltration 5 times. The final product was redissolved in phosphate-buffered saline (PBS) and stored at 4°C to avoid freezing. Then, the GrB peptide–GQD probe was added to B-PDA (0, 0.02, 0.05, 0.10, 0.15, and 0.20 mg mL^{-1}) and stirred overnight in the dark. The GrB peptide–GQD samples were loaded onto the B-PDA by physical adsorption and formed the final product BP-PDA, which was stored at 4°C.

BP-PDA bionanoprobe for *in vitro* GrB detection. To optimize the quenching efficiency (Qe) of the nanoparticle, PDA-PEG dispersion was first sonicated for 20 min in an ice bath to obtain a homogeneous solution. Then 200 nM P_{GQD} was incubated PDA-PEG (0-200 μg mL^{-1}) and gently stirred from for 30 min at room temperature. Then fluorescence emission spectra of each sample were measured from 580 nm to 800 nm at the excitation of 560 nm. Qe was calculated according to the equation: $Qe = (F_0-Fq)/F_0$, where F_0 represents the fluorescence intensity of P_{GQD} without quenching, Fq represents the fluoresce intensity quenched by PDA.

In the GrB detection experiment, concentration of PDA and P_{GQD} was optimized at 0.15 μM and 100 μg/mL, respectively to ensure a high Qe (>95%). Then GrB targeted with a gradient concentration of 0-1.00 μM was incubated into the BP-PDA dispersion and kept at 37℃ for 1 h for sufficient GrB cleavage activity. Then fluorescence of each group was measured and quantified analyzed. Limit of detection (LOD) of BP-PDA bionanoprobe was calculated according to the equation: $LOD = 3\sigma/k$, where σ represents the standard deviation of the noise, and k represents the slope of the calibration curve of detection. Specificity of BP-PDA bionanoprobe was investigated by incubating the 0.15 μM GrB,granzyme A (GrA), matrix metalloproteinase-2 (MMP-2), and glutathione (GSH) under the same assay conditions above. Three independent experiments were performed for each measurement.

Biocompatibility studies of BP-PDA. THP-1 and HL-60 cells were grown in 96-well plates at 2.5×10^3 cells/well in 100 μL RMPI 1640 and Ea.hy926 cells were grown in 100 μL of DMEM sup-plemented with 10% FBS [5]. Different concentrations of PDA and PDA–PEG (50 mg mL^{-1}–200 mg mL^{-1}) were added to the cells. PEI (1 mg mL^{-1}), a known cyto-toxic cationic polymer, was used as a positive control. Cells were treated with nanoparticles for 12 or 24 h and then 10 μL of CCK8 reagent was added to each well. After incubation for 4 h at 37 °C in 5% CO_2, the absorbance of the formazan product was measured at 490 nm using a Biotek Synergy HT plate reader (Winooski, VT). The percentage viability of cells was expressed as the ratio of absorbance of polymer-treated cells relative to the negative control (0 mg mL^{-1}) × 100 and plotted as a function of the polymer concentration.

The effect of PDA–PEG on cell activity was tested using the LIVE/DEAD™ Cell Imaging Kit (488/570). THP-1 cells were grown in 96-well plates at 2.5×10^3 cells/well in 100 μL of RMPI 1640 supplemented with 10% FBS. PDA or PDA–PEG (50 mg mL^{-1}) was added to the cells and cocultured for 24 h. Using the LIVE/DEAD™ Cell Imaging Kit, live cells were distinguished by the presence of ubiquitous intracellular esterase activity as determined by the enzymatic conversion of the virtually nonfluorescent cell permeant calcein AM to the intensely fluorescent calcein, which is well-retained within live cells. In contrast, in dying and dead cells a bright red fluorescence was generated upon binding to DNA.

BP-PDA based ICB therapy. The humanized AML mice were given LILRB4 mAb, PDA–PEG, B-PDA (equivalent to 2.5 mg kg^{-1} of Ab), BP-PDA (equivalent to 2.5 mg kg^{-1} of Ab), or control PBS intravenously 7 d after THP-1 cell implantation and were treated every other day with five consecutive injections. The tumor size for all groups was determined using caliper measurements (width × width × length). At the therapeutic endpoint, blood was collected for a biochemistry test. Hematoxylin staining and immunostaining were performed on paraffin sections of tumors, hearts, spleens, lungs, kidneys, and livers. Antibodies against CD3 (Abcam, ab135372, 1:150) and CD8 (Invitrogen, MA514548, 1:100) were used. To track the distribution of nanoparticles, the mice were treated with FITC@PDA-PEG or FITC@B-PDA, and after 24 h, the kidneys, lungs, spleen, liver, heart, and tumor under the skin were assessed by *in vitro* imaging. The images were visualized using a fluorescence microscope (BX43, Olympus, Japan) and viewed using CellSens Standard imaging software (Olympus, Japan).

***In vivo* fluorescence imaging.** To determine the immune response induced by BP-PDA, the GrB signal was measured based on real-time GQD imaging by luminescence imaging day 1, 5, 9, 13, 17. The treatments were injected every alternate day for a total of five dosages and fluorescence measurements were performed using a PerkinElmer IVIS spectrum system. Fluorescence imaging of living animal was performed every 24 h after the injection by using the In vivo imaging system (IVIS). The *in vivo* GQD fluorescence images were captured and analyzed using Living Image Software.

Excitation and emission filters were settled as 520 nm and 640 nm, respectively.

RESULTS AND DISCUSSION

Mechanisms of BP-PDA bionanoprobe for ICB therapy and immune marker detection. Based on the excellent potential for surface modification and optical absorbance of PDA nanoparticles, we designed PDA as an integrated nanocomposite for ICP-blocker loading and GrB sensing. As showed in **Scheme 1A**, PDA nanoparticles were self-polymerized by naturally derived dopamine from the human body, a derivative of 3,4 dihydroxy-L-phenylalanine (DOPA)[10, 15]. The nanoparticles were PEGylated first (denoted as PDA-PEG) to improve their distribution and stability in the blood-stream. PDA–PEG was then conjugated with LILRB4 mAb blocker to form B-PDA, via the typical EDC/NHS chemistry to target the LILRB4 overexpressed AML cells and block the LILRB4 ICP.

To detect GrB activated by ICB therapy in real-time, a biocompatible FRET nanoprobe was designed using PDA (acceptor) and organic fluorescent GQD (donor). Carbon-derived GQD showed advances on good biocompatibility, feasibility for surface functionalization, and good photostability [16,17]. GQD was labeled on the GrB-cleavable peptide (P_{GQD}) and then loaded onto PDA-PEG via π-π interactions to form BP-PDA [18]. GQD fluorescence was quenched by PDA to make the "SIGNAL OFF" via "FRET." The BP-PDA bionanoprobe was then injected into the humanized AML mouse via the caudal vein and targeted AML cells to block LILRB4 expression, which induced CTLs to secrete GrB in the AML cells (**Scheme 1B**) [19]. GrB would cleave its recognizing peptide and detach GQDs from PDA and turn to "SIGNAL ON."

Scheme 1. Preparation process of the blocker and P_{GQD} loaded PDA (BP-PDA) bionanoprobe and its application for acute myeloid leukemia (AML) immune checkpoint blockage and immune marker detection. (A) Fabrication of the BP-PDA bionanoprobe and (B) BP-PDA-based ICB therapy and granzyme B detection in humanized AML mouse.

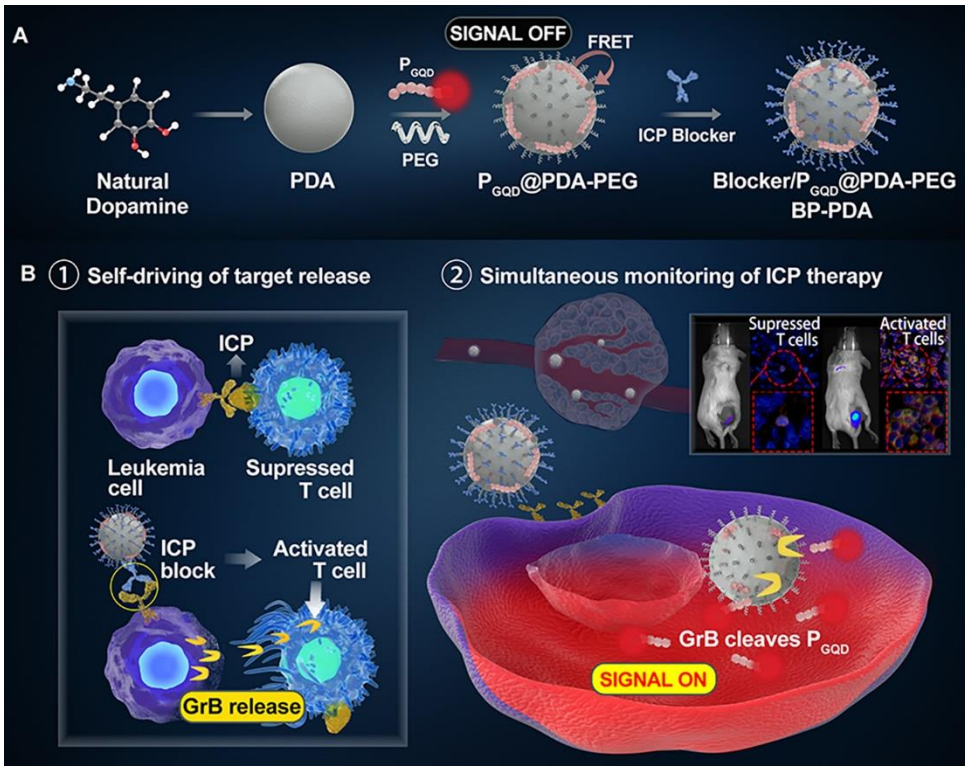

Establishment of BP-PDA bionanoprobe. To detect GrB *in vivo*, we designed a highly biocompatible organic FRET probe using PDA quencher and GQD donor. PDA was synthesized via a simple self-polymerization method and PEGylated as mentioned previously [3]. The spherical morphology of the nanosized PDA and GQD was imaged using TEM (**Figure 1A**). A short peptide (GK-IEPD-APC) sequence which can be cleaved by GrB was labeled with red fluorescent GQD and adsorbed onto PDA via π-π interactions [8]. A high quenching efficiency of the acceptor is important pre-condition for FRET assay. To optimize the Qe of BP-PDA nanoprobe, PDA was coupled with P_{GQD} of varying concentrations from 0-200 μg mL^{-1}. Qe can reach up to 96.6 ± 0.7 % for 100 nM of GQD labeled peptide incubated with 200 μg mL^{-1} of PDA, which ensured a low background detection signal (**Figures 1B, C**).

The LILRB4 mAb blocker was modified on PEGylated PDA via typical EDC/NHS chemistry. To investigate the successful construction of the BP-PDA, average hydrodynamic diameters of PDA, PDA-PEG, and BP-PDA were first characterized (**Figure S1**). ζ potentials of BP-PDA negatively shifted to -19.5 mV (**Figure 1D**). UV-vis spectra revealed that B-PDA had broad absorption bands from 200 to 700 nm, and slightly enhanced around 650 nm (**Figure 1E**), which could better cover the fluorescence emission of GQD (emission peak at 641 nm). X-ray photoelectron spectroscopy (XPS) showed that after LILRB4 mAb blocker and P_{GQD} modification, peak of C-O, C-N shifted to lower binding energy of 283 eV (**Figures 1F**). The peak of sulfur (around 160 eV) revealed in BP-PDA indicated the present of the peptide molecules (**Figure S2**) [20]. In FTIR spectra (**Figure S3)**, BP-PDA displayed characteristic bands at 2923 cm^{-1} and 1018 cm^{-1} assigned to the stretching vibrations of C-H and C-O from the PEG chain [21]. Altogether, these results indicated of the successful constructions of the BP-PDA nanoprobe.

In blood circulation, nanoparticles with lower surface stability may easily adsorb various proteins and form a protein corona structure [22]. Herein, PDA, PDA–PEG, and BP-PDA were incubated with water, PBS, DMEM, and 20% FBS containing PBS buffer.

There was no notable change on hydrodynamic diameters of BP-PDA even for 12 d (**Figure 1G**). Bovine serum albumin contained buffer also did not considerably change the hydrodynamic diameter and polydispersity of BP-PDA, which ensured its good stability for further *in vivo* use (**Figure S4**) [10]

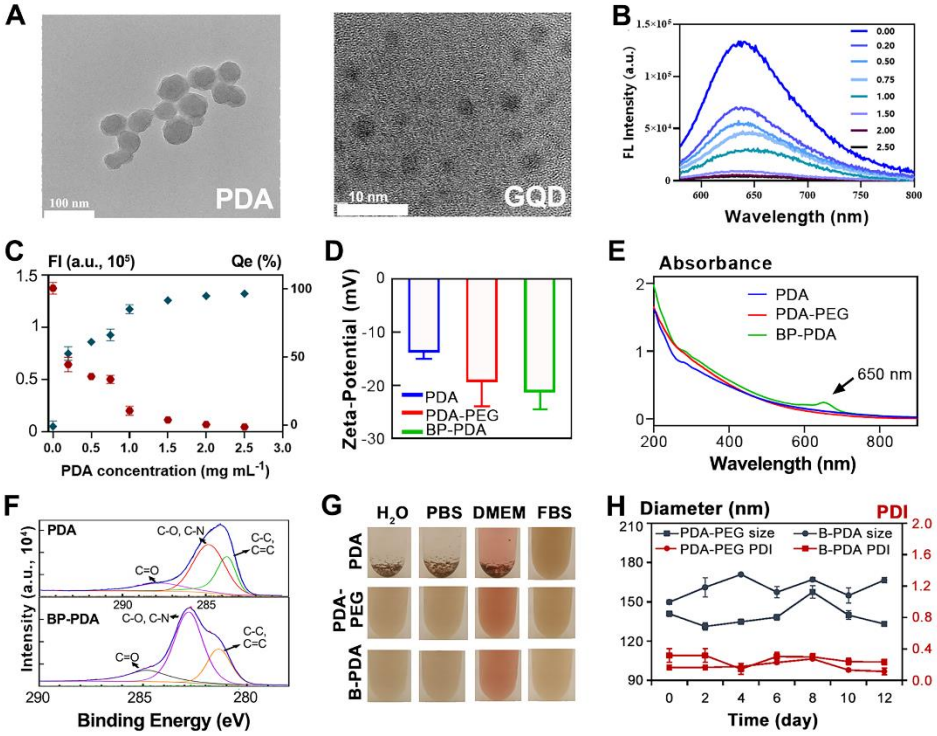

Figure 1. Characterizations of polydopamine (PDA), PDA–polyethylene glycol (PEG), and B-PDA-probe (BP-PDA). (A) Transmission electron microscopy image of PDA and GQD; (B) Photoluminescence spectrum of recovery fluorescence for P-PDA incubated with GrB probe in different concentration (0–1.00 μM); (C) Fluorescence intensity and quenching efficiency of granzyme B (GrB) probe incubated with differentially concentrated PDA–PEG (0–0.20 mg mL^{-1}); (D) ζ potential of PDA, PDA-PEG, BP-PDA by DLS; (E) Ultraviolet–visible absorptions of PDA, PDA–PEG, and BP-PDA; (F) X-ray photoelectron spectra of PDA and BP-PDA; (G) Images of PDA, PDA–PEG, and BP-PDA suspended in water, phosphate-buffered saline (PBS), Dulbecco's modified Eagle's medium, and 20% fetal bovine serum for 24 h; (H) The hydrodynamic diameter of PDA–PEG and BP-PDA as a function of time in PBS buffer (PDI:).

Sensitivity and septicity of BP-PDA toward GrB.

The sensing ability of BP-PDA bionanoprobe for GrB detection *ex vivo* was performed in **Figure 2A**. First, we optimized that BP-PDA showed a maximal fluorescent intensity after 1 h of incubation at 37 ℃ to ensure the entire GrB cleveage process. Next, GrB with a series of concentration from 0 - 1.0 μM was incubated the BP-PDA with fixed concentration of 100 nM for 1 h. The peak fluorescent intensity at 641 nm exhibited good linear relationship with the logarithmic concentrations of GrB (**Figure 2B**). Limit of the detection (LOD) was calculated at 38 nM with R^2 = 0.951) which was comparable to the reported concentrations that can induce target cell death [23,24] (**Figure 2C**). Then, we investigated the sensing specificity of BP-PDA bionanoprobes against GrB,granzyme A (GrA), matrix metalloproteinase-2 (MMP-2), and glutathione (GSH). It showed that the fluorescence of BP-PDA bionanoprobes did not significantly increased in presence of non-GrB target (*P* <0.01), indicating the high selectivity of BP-PDA to GrB which could be minimal interfered by the non-specific biomolecules (**Figure 2D**).

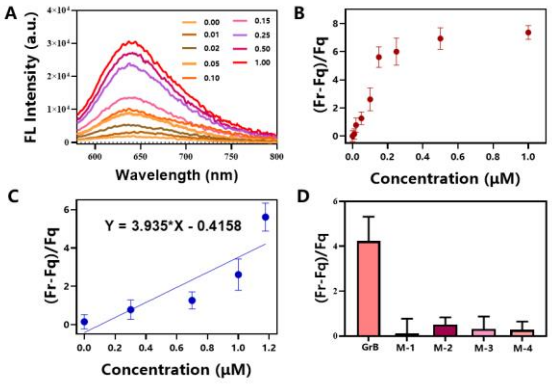

Figure 2. Detection of GrB *in vitro*. Photoluminescence spectra (A) and Relative fluorescence intensity (B) BP-PDA incubated with GrB of various concentrations from 0-1 μM. (Fr represents the fluorescence intensity of BP-PDA bionanoprobe after GrB incubation; Fq represents the fluorescence intensity of BP-PDA without target addition); (C) Linear relationship fitting between the relative fluorescence intensity and the GrB concentrations ranging from 0 - 0.15 μM; (D) Relative fluorescence intensity of BP-PDA incubated with against GrB, granzyme A (GrA), matrix metalloproteinase-2 (MMP-2), and glutathione (GSH) at a concentration of 0.15 μM. Data were expressed as mean ± standard deviation (n = 3) and analyzed by t-test. Data represented as mean ± standard deviation (n

= 3) and analyzed by t-test for two groups comparison and one-way ANOVA for three groups comparison.

***In vitro* and *in vivo* biocompatibility of BP-PDA**. Excellent biocompatibility of this organic quencher and donor based FRET bionanoprobe is the prerequisites for its physiological application. Consequently, we investigated the *in vitro* cytotoxicity of PDA towered two typical amyloid leukemia cell lines (THP-1 and HL-60) and the normal human umbilical vein cell (Ea.hy926), which abundantly present in the endothelium of blood vessels of AML patients. **Figure 3A** showed that cell viability rates of the three cell lines exceeded around 97% in PDA-PEG incubated groups (up to 200 μg mL^{-1}). Compared with PEI-incubated cells, which is a polycation widely used for *in vitro* and *in vivo* drug or gene delivery, the PDA- and PDA–PEG-incubated groups showed significantly higher viability rates (*P*s < 0.001). PDA-PEG also performed a high biosafety in the live/dead assay of THP-1 cells (**Figures 3B, C**). The hemolysis assay showed that compared with PEI, the hemolytic activity of PDA–PEG in RBCs was relatively low (<5%) even at the highest concentration of 400 μg mL^{-1}(**Figure 3D)**, suggesting the high safety of intravenously injected PDA nanomaterials [25].

Next, we systematically investigated the biosafety of BP-PDA bionanoprobe *in vivo*. BP-PDA treatment was carried out according the protocol in experiment section. First, no significant change was observed between the control and BP-PDA-treated mice on body weights of mice during BP-PDA treatment (**Figure 3E**), in which no significant change was observed between the control and BP-PDA-treated mice. ICB treatment may cause uncontrolled collateral effects, leading to immune-related adverse events (irAEs) [26, 27]. Second, biochemical analysis of the serum was used to evaluate the function of major organs and tissues (**Figure 3F**), including the alanine aminotransferase, aspartate aminotransferase, blood urea nitrogen (BUN), and creatine kinase (CK) levels [28]. There were no significant differences in the levels of the four markers in each group (*P*s > 0.05). However, LILRB4 mAb-treated mice showed slightly higher levels of BUN and CK, which may be because of pure mAb-induced irAEs. The *in vivo* biodistribution of the nanocomposites was also evaluated. To avoid the effects of fluorescent nanoprobes on tumors, B-PDA was only labeled with FITC on its outer layer (FITC@B-PDA) and injected via the tail vein (**Figure 5G**). Fluorescence images of the heart, liver, spleen, lungs, kidneys, and tumor were collected 24 h after injection (**Figure 5H**). FITC@B-PDA mainly accumulated in tumors (**Figure 5I**). Additionally, FITC@B-PDA accumulation in the liver and kidneys was lower than that of FITC@PDA–PEG, indicating the tumor-targeting capability of LIRLB4 mAb modified on PDA. Finally, we analyzed tissue sections of the main organs, including the heart, liver, kidney, spleen, and lungs (**Figures 3J, S5**), in which no pathological damage was observed.

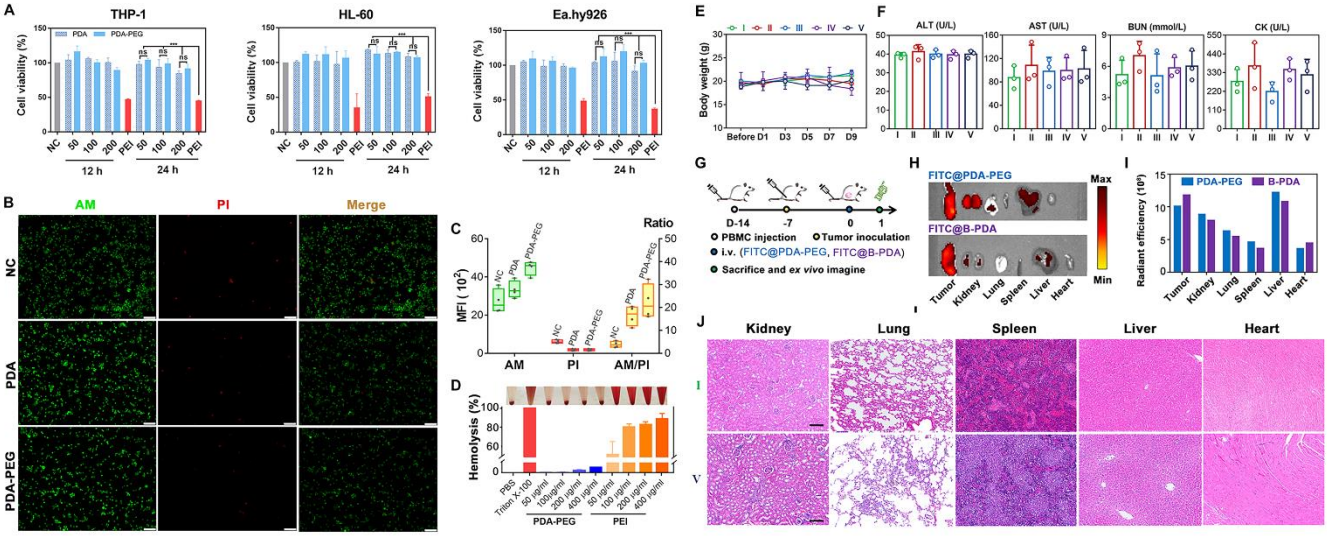

Figure 3. *In vitro* and *in vivo* biosafety of polydopamine (PDA), PDA–polyethylene glycol (PEG), and B-PDA. (A) The survival rate of THP-1 cells, HL-60, and Ea.hy926 after the treatment with different concentrations of PDA and PDA-PEG; (B) Live/dead cells imaging of THP-1 cells after coculture with PDA and PDA-PEG after 24 h (scale bar: 75 μm); (C) The mean fluorescence intensity of live cells and dead cells and its ratio; (D) Image of the hemolysis rate after treatment with different concentrations of PDA–PEG, with polyethyleneimine as the positive control; (E) Body weight changes of humanized AML mice during the treatment process (I, PBS; II, LILRB4 mAb; III, PDA-PEG; IV, B-PDA; and V, BP-PDA); (F) Blood parameters of mice after treatment, including alanine aminotransferase (ALT), aspartate aminotransferase (AST), blood urea nitrogen (BUN), and creatine kinase (CK); (G) Schematic illustration of the *ex vivo* fluorescence imaging protocol; (H) *Ex vivo* fluorescence images of tumors and organs (kidneys, lungs, spleen, liver, and heart) after injection of fluorescein 5-isothiocyanate (FITC)-labeled polydopamine (PDA)–polyethylene glycol and FITC-labeled B-PDA groups; (I) Quantification of the fluorescence intensity of tumors and organs. Data represented as mean ± standard deviation (n = 3); (J) Hematoxylin and eosin staining of main organs of mice after different treatments (Scale bars: 100 μm); Data represented as mean ± standard deviation (n = 3) and analyzed by t-test for two groups comparison and one-way ANOVA for three groups comparison.

ICP blockage and GrB detection in living cells. We next investigated the self-driving of the LILRB4 blockage of BP-PDA bionanoprobes. First, the original LILRB4 level of the cells was analyzed by flow cytometry, where LILRB4 was highly expressed in THP-1 cells at a positive rate of ~99.5%, whereas the HL-60 and Ea.hy926 cells showed negative expression (**Figures 4A, B**).Then FITC was labeled on the PEG terminal and modified on the BP-PDA (FITC@BP-PDA) to track the cellular uptake efficiency. FITC@B-PDA showed around five folds higher intracellular fluorescence in THP-1 cells than the other two cells (*P* < 0.05, **Figures 4C**), which indicated the specific targeting ability of B-PDA to LILRB4-overexpressed THP-1 cells. Time for cellular uptake was investigated in **Figure S6** which showed 4 h of incubation could ensure an efficient cellular uptake of BP-PDA to THP-1 cells. Subsequently, the avidity of B-PDA to the surface LILRB4 protein in THP-1 cells was analyzed by flow cytometry (**Figure 3F**). A

concentration-dependent interaction between B-PDA and LILRB4 was carried out. B-PDA at a concentration of 80 μg mL^{-1} effectively blocked LILRB4 expression in THP-1 cells, and their reaction could enter the equivalence zone [29]. Higher or lower concentrations of B-PDA (40 or 120 μg mL^{-1}) did not block the surface LILRB4 protein, as immune precipitation (antibody–antigen complexes) can be prevented by an excess of antigen or antibody.

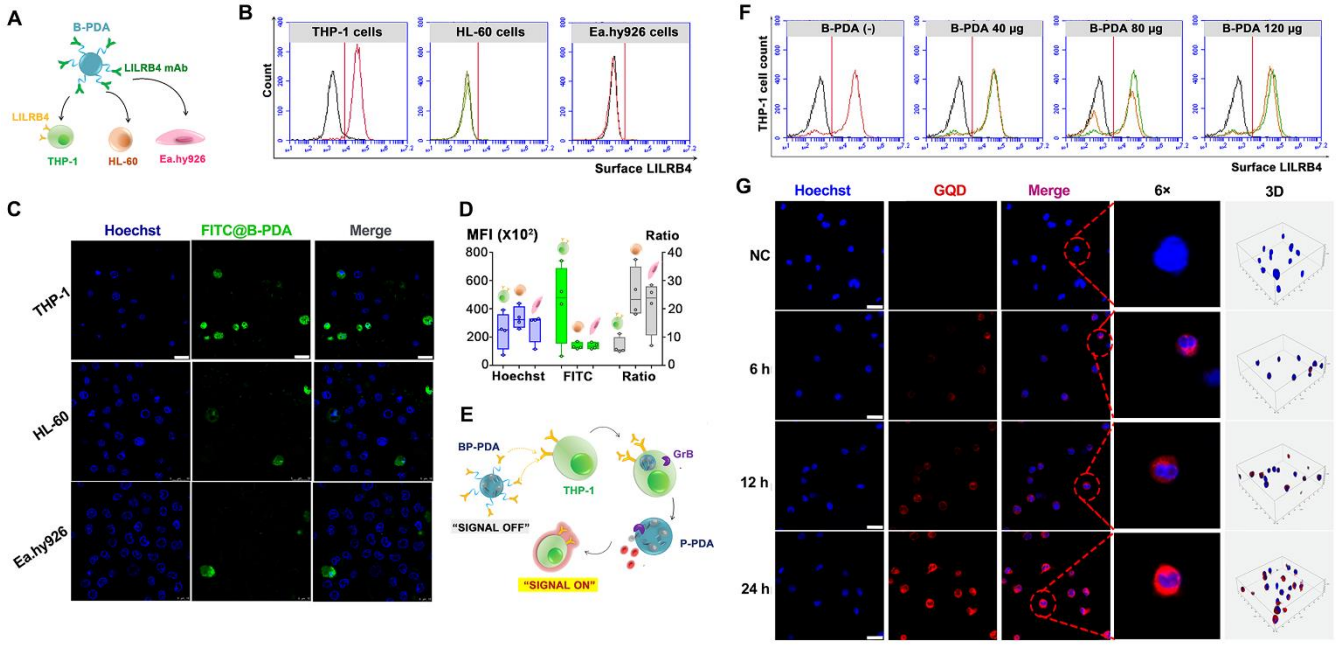

Figure 4. Blocker of the immunity globulin-like receptor B4 (LILRB4) level and uptake of B-polydopamine (PDA) *in vitro*. (A) Schematic diagram of the interaction between B-PDA and the three cell lines (THP-1, HL-60, and Ea.hy926 cells); (B) LILRB4 levels in the three cell lines by flow cytometric analysis; (C) Cellular uptake of Fluorescein 5-isothiocyanate (FITC)-labeled B-PDA (FITC@B-PDA) by THP-1, HL-60, and Ea.hy926 cells after 12 h of coculture (scale bar: 10 μm) and fluorescence analysis (D); (E) Schematic diagram of BP-PDA action *in vitro* and *in vivo*; (F) Flow cytometric analysis of THP-1 cells (1×10^6) incubated with 40, 80, or 120 μg mL^{-1} of B-PDA for detecting LILRB4 surface domain of THP-1 cells; (G) *In vitro* fluorescence images of THP-1 cells cocultured with BP-PDA with or without granzyme (GrB) (scale bar: 10 μm).

GrB has been identified as a robust predictor of immunotherapy response and is widely applied in the diagnosis of treatment effectiveness [30]. We first investigated the *in vitro* GrB minoring ability of BP-PDA. THP-1 cells were treated with GrB and incubated with BP-PDA for 6, 12, and 24 h (**Figure 5G**). BP-PDA-incubated THP-1 cells showed a time-dependent fluorescence intensity, in which 6 h of detection exhibited visible fluorescence recovery ($1.7 \pm 0.9 \times 10^4$).

Self-driving of *in vivo* ICP blockage by BP-PDA LILRB4, as the novel ICP for AML and the myeloid inhibitory receptor, was reported to block and hence interrupt the development of monocytic AML heterogenic immune response [31-33]. We first investigated the therapeutic effect of LILRB4 blocking induced by BP-PDA in AML. A humanized model was first constructed by the intravenous injection of human peripheral blood mononuclear cells (PBMCs) into non-obese diabetic/severe combined immunodeficiency IL2Rγnull (NSG) mice. The design of animal study was showed in **Figure 5A**. One-week post-implantation of PBMCs, 1×10^6 THP-1 cells were subcutaneously implanted in the mouse. To confirm the establishment of the humanized AML model, the engraftment of human T cells and the proportion of THP-1 cells in the tumor were analyzed by flow cytometry using APC-labeled hCD45, FITC-labeled hCD11b, and PE-labeled hCD14 antibodies (**Figure S7**). Two weeks after PBMCs implantation, around 20% to 30% of human T cells were engrafted into the mice. The proportion of THP-1 cells in tumor tissue to total cells ranged from 61.4% to 87.6%, suggesting that the humanized AML mouse model was successfully established (**Figure S8**). When the average tumor size of the humanized AML mice reached approximately 100 mm^3 (marked as day 0), the mice were randomly divided into five groups (n=3): I, PBS; II, LILRB4 mAb; III, PDA-PEG; IV, B-PDA; and V, BP-PDA. The mice were injected with the corresponding formulations twice a week for a total of five times. The doses of LILRB4 mAb and PDA nanoparticles were 2.5 mg kg^{-1} and 100 μg kg^{-1}.

B-PDA and BP-PDA showed similar levels of ICP blocking to LILRB4 mAb, suppressing the tumor size effectively (**Figures 5B, C**). At the end of the therapy (day 16), the tumor inhibition rates for the three groups reached 70.6%, 89.5%, and 88.8%, respectively. Simultaneously, a significant reduction in the tumor weight in the mAb-containing groups (IV and V) was found when compared to group I (*P*s <0.001, **Figure 5D**). Next, tumor sections from each group were stained with Ki67 and TUNEL to observe the degree of tumor proliferation and damage in the corresponding groups (**Figure 5E**). Comparatively, tumor sections from group IV or V exhibited notably decreased leukemia development compared with that of the PBS group (**Figure 5F, G**). These results indicated the effective ICP therapy in AML mice model induced by the BP-PDA bionanoprobe.

Herein, tumor suppression comparable to that of a previous study was obtained in the BP-PDA-treated group even with a smaller dosage of LILRB4 mAb [34]. This may be related to the enhanced permeability and retention (EPR) effect of nanoparticles, which promotes greater nanoparticle permeability in tumor vessels than in normal vessels compared to macromolecules and retains macromolecules in tumors owing to their poor lymphatic clearance [35]. The EPR effect may not only benefit the *in vivo* monitoring of the bionanoprobe, but also offer ICB therapy with lower dose of inhibitor compared with the conventional inhibitor treatment method.

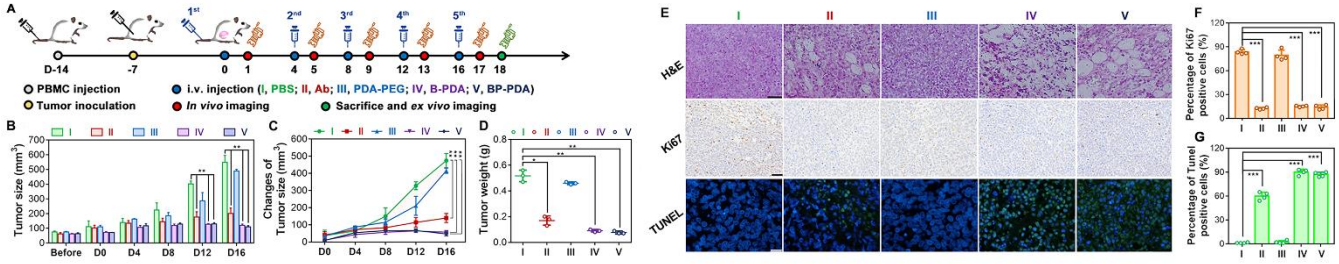

Figure 5. Therapeutic effect of nanoparticles on humanized acute myeloid leukemia mice. (A) Schematic illustration of the treatment protocol; (B) Tumor size in mice under different treatment conditions (n = 3); (C) Changes in tumor size under different treatment conditions (n = 3); (D) Tumor weight curve of each treatment group; (E) Hematoxylin-and-eosin- (scale bar: 50 μm), Ki67- (scale bar: 50 μm), and terminal deoxynucleotidyl transferase deoxyuridine triphosphate nick end labeling (TUNEL)- (scale bar: 20 μm) stained tumors sections of different groups; Quantitative analysis of Ki67 (F) and TUNEL (G) in tumor tissue sections; Data represented as mean ± standard deviation. * $P < 0.05$, ** $P < 0.01$, and *** $P < 0.001$.

***In situ* GrB monitoring in living animal.** LILRB4 known as a transmembrane protein that inhibits adaptive immune responses mediated by CTLs, achieved a blocking strategy for T-cell-independent anticancer strategies [36,37]. Thus, we investigated the CTL recruitment around tumors via CD3 and CD8 co-staining to confirm the immune response induced by the blocker loaded PDA groups (B-PDA). To avoid the fluorescence interference of P_{GQD}, only B-PDA was used for immune staining. As shown in **Figure 6A**, B-PDA treatment resulted in significantly increased numbers of engraftable CTLs (CD3+CD8+) in the tumor tissues than the control group (MFI: 3.8×10^3 and 7.7×10^3, $P<0.05$). This observation agrees well with previous findings that LILRB4 signaling in monocytic AML cells suppresses T-cell-medicated antitumor immunity [38, 39].

We subsequently characterized the efficacy of BP-PDA bionanoprobes for real-time and *in situ* monitoring of GrB in humanized AML model. Injection of BP-PDA bionanoprobe was performed on day 0, 4, 8, 12, 16. Fluorescence imaging of living animal was performed every 24 h after the injection by using the In vivo imaging system (IVIS) (**Figure 6B**). As showed in **Figure 6C**, from the day 1 of BP-PDA treatment, obverse red fluorescence signal can be detected in the tumor area. To examine wither the fluoresce signal is specific induced by the GrB detection from BP-PDA bionanoprobe, fluorescence signal of mice treated with BP-PDA was compared with that of B-PDA treated mice at day 1, 5, 9, 13, 17. It showed that signals of BP-PDA treated mice were significantly higher than that of P-PDA ($P<0.01$, **Figure 6D**). Tumor volumes of mice were also analyzed to assess the anti-tumor effect at the same time points above (**Figure 6E**). It showed that a higher immune response with stronger fluoresce signal corresponded to a more effective anti-tumor efficiency. These results indicated this multifunctional bionanoprobe showed effective ICB therapy and real-time *in vivo* monitoring of related immune responses. The self-reporting BP-PDA nanoplatform with multiple functions offered a much earlier assessment of immunotherapy than measuring tumor volume after anatomy. This integrated delivery mode avoids repeated drug and probe injections, which may be conducive to obtaining a timely response within the best therapeutic effect evaluation window.

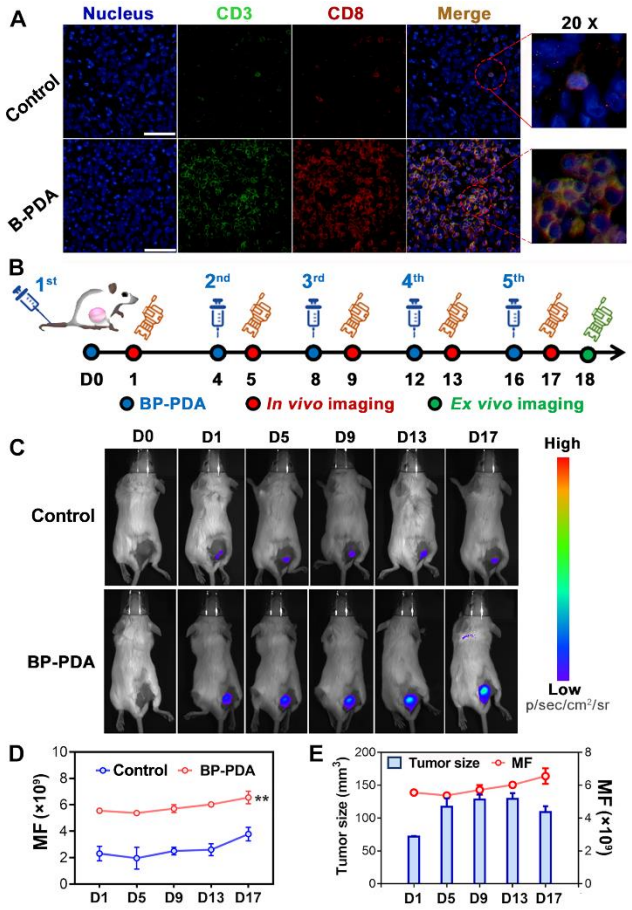

Figure 6. Real-time monitoring of the effect of B-polydopamine-probe (BP-PDA) on humanized acute myeloid leukemia mice. (A) Immunofluorescence images of CD3/CD8 in tumor sections from mice with their corresponding treatments: control (PDA-PEG) and B-PDA groups (scale bar: 50 μm); (B) Schematic diagram of BP-PDA *in vivo* fluorescence imaging of mice; (C) *In vivo* live imaging of mice injected with control (P-PDA) or BP-PDA at different time points; (D) Quantification of mean fluorescence of BP-PDA; (E) Correlation analysis of tumor size and mean fluorescence after BP-PDA injection at different time points.

CONCLUSION

In this study, we designed a multifunctional immunotherapy and therapeutic effect-monitoring system based on natural PDA nanomaterials and organic fluorescence quantum dots. The proposed system effectively blocked a new ICP target in the AML model and sensitively detected the key immune activation biomarker *in vivo*. PDA, a highly biocompatible nanomaterial, not only served as an ICB agent carrier but also as a quencher to form "FRET" paired with GQD. BP-PDA offered sensitive GrB detection *in vitro*. It realized intracellular detection of GrB at 6 h and in *vivo* detection at the early stage of ICB therapy. This "all-in-one" comprehensive nanocomposite hence shows good potential for ICB therapy in AML and warrants future clinical validation.

ASSOCIATED CONTENT

Supporting Information

The Supporting Information is available free of charge on the ACS Publications website.

TEM of PDA-PEG (PDF)
TEM image (A) and potential (B) of GQD (PDF)
Live/dead cell imaging of PDA-PEG in THP-1 cells at different time points (PDF)
Confirmation of humanized AML model (PDF)

AUTHOR INFORMATION

Corresponding Authors

Gerile Oudeng *- Department of Hematology and Oncology, Shenzhen Children's Hospital of Shantou University Medical College, Futian, Shenzhen, Guangdong, 518026, PR China; Email: gerile.oudeng@connect.polyu.hk*

Feiqiu Wen *- Department of Hematology and Oncology, Shenzhen Children's Hospital of Shantou University Medical College, Futian, Shenzhen, Guangdong, 518026, PR China; Email: fwen62@126.com*

Mo Yang

Department of Biomedical Engineering, Hong Kong Polytechnic University, Hung Hom, Kowloon, 999077 Hong Kong SAR, PR China

Authors

Dangui Zhang: Department of Hematology and Oncology, Shenzhen Children's Hospital of Shantou University Medical College, Futian, Shenzhen, Guangdong, 518026 PR China;

Research Center of Translational Medicine, Second Affiliated Hospital of Shantou University Medical College, Shantou, Guangdong, 515041 PR China

Honglian Wu: Department of Biomedical Engineering, Hong Kong Polytechnic University, Hung Hom, Kowloon, 999077 Hong Kong SAR, PR China

Tianci Wang: Department of Hematology and Oncology, Shenzhen Children's Hospital of Shantou University Medical College, Futian, Shenzhen, Guangdong, 518026 PR China;

Yuting Wang: Department of Hematology and Oncology, Shenzhen Children's Hospital of Shantou University Medical College, Futian, Shenzhen, Guangdong, 518026 PR China;

Sixi Liu: Department of Hematology and Oncology, Shenzhen Children's Hospital of Shantou University Medical College, Futian, Shenzhen, Guangdong, 518026 PR China.

Author Contributions

The manuscript was written through contributions of all authors. All authors have given approval to the final version of the manuscript.

Notes

The authors declare no competing financial interest.

ACKNOWLEDGMENT

The research was supported by Shenzhen Science and Technology Program (SGDX20201103095404018) and Shenzhen Fund for Guangdong Provincial High Level Clinical Key Specialties (SZGSP012).

REFERENCES

1. Yi M, Li A, Zhou L, Chu Q, Song Y, Wu K. The global burden and attributable risk factor analysis of acute myeloid leukemia in 195 countries and territories from 1990 to 2017: estimates based on the global burden of disease study 2017. J Hematol Oncol. 2020; 13: 72.

2. Newell LF, Cook RJ. Advances in acute myeloid leukemia. BMJ. 2021; 375: n2026.

3. Acheampong DO, Adokoh CK, Asante DB, Asiamah EA, Barnie PA, Bonsu DOM, et al. Immunotherapy for acute myeloid leukemia (AML): a potent alternative therapy. Biomed. Pharmacother. 2018; 97: 225-32.

4. Hodi FS, O'Day SJ, McDermott DF, Weber RW, Sosman JA, Haanen JB, et al. Improved survival with ipilimumab in patients with metastatic melanoma. N. Engl. J. Med. 2010; 363: 711-23.

5. Graff JN, Chamberlain ED. Sipuleucel-T in the treatment of prostate cancer: an evidence-based review of its place in therapy. Core Evid. 2015; 10: 1-10.

6. Jiang Y, Chen M, Nie H, Yuan Y. PD-1 and PD-L1 in cancer immunotherapy: clinical implications and future considerations. Hum Vaccin Immunother. 2019; 15: 1111-22.

7. Ribas A, Wolchok JD. Cancer immunotherapy using checkpoint blockade. Science. 2018; 359: 1350-5.

8. Vaddepally RK, Kharel P, Pandey R, Garje R, Chandra AB. Review of indications of FDA-approved immune checkpoint inhibitors per NCCN guidelines with the level of evidence. Cancers (Basel). 2020; 12.

9. Li Z, Deng M, Huang F, Jin C, Sun S, Chen H, et al. LILRB4 ITIMs mediate the T cell suppression and infiltration of acute myeloid leukemia cells. Cell. Mol. Immunol. 2020; 17: 272-82.

10. Zappasodi R, Merghoub T, Wolchok JD. Emerging concepts for immune checkpoint blockade-based combination therapies. Cancer Cell. 2018; 34: 690.

11. Flavell RR, Evans MJ, Villanueva-Meyer JE, Yom SS. Understanding response to immunotherapy using standard of care and experimental imaging approaches. Int J Radiat Oncol Biol Phys. 2020; 108: 242-57.

12. Nicolai CJ, Raulet DH. Killer cells add fire to fuel immunotherapy. Science. 2020; 368: 943-4.

13. Hiebert PR, Granville DJ. Granzyme B in injury, inflammation, and repair. Trends Mol Med. 2012; 18: 732-41.

14. Alghamri MS, Nunez FJ, Kamran N, Carney S, Altshuler D, Lowenstein PR, et al. Functional characterization of tumor antigen-specific T-cells isolated from the tumor microenvironment of sleeping beauty induced murine glioma models. Meth. Enzymol. 2020; 631: 91-106.

15. Nguyen A, Ramesh A, Kumar S, Nandi D, Brouillard A, Wells A, et al. Granzyme B nanoreporter for early monitoring of tumor response to immunotherapy. Sci Adv. 2020; 6(40):eabc2777.

16. Jiang C, Wang Y, Wang J, Song W, Lu L. Achieving ultrasensitive in vivo detection of bone crack with polydopamine-capsulated surface-enhanced Raman nanoparticle. Biomaterials. 2017; 114: 54-61.

17. Zhan Q, Shi X, Zhou J, Zhou L, Wei S. Drug-controlled release based on complementary base pairing rules for photodynamic-photothermal synergistic tumor treatment. Small. 2019; 15: e1803926.

18. Batul R, Tamanna T, Khaliq A, Yu A. Recent progress in the biomedical applications of polydopamine nanostructures. Biomater Sci. 2017; 5: 1204-29.

19. Li H, Jia Y, Peng H, Li J. Recent developments in dopamine-based materials for cancer diagnosis and therapy. Adv Colloid Interface Sci. 2018; 252: 1-20.

20. Liu M, Zeng G, Wang K, Wan Q, Tao L, Zhang X, et al. Recent developments in polydopamine: an emerging soft matter for surface modification and biomedical applications. Nanoscale. 2016; 8: 16819-40.

21. Liu Y, Ai K, Lu L. Polydopamine and its derivative materials: synthesis and promising applications in energy, environmental, and biomedical fields. Chem Rev. 2014; 114: 5057-115.

22. Wang Z, Duan Y, Duan Y. Application of polydopamine in tumor targeted drug delivery system and its drug release behavior. J Control Release. 2018; 290: 56-74.

23. Facure MHM SR, Mercante LA, Correa DS. A review on graphene quantum dots and their nanocomposites: from laboratory synthesis towards agricultural and environmental applications. Environ Sci: Nano. 2020; 7: 3710-34.

24. Ishikawa-Ankerhold HC, Ankerhold R, Drummen GP. Advanced fluorescence microscopy techniques--FRAP, FLIP, FLAP, FRET and FLIM. Molecules. 2012; 17: 4047-132.

25. Lu H, Li W, Dong H, Wei M. Graphene quantum dots for optical bioimaging. Small. 2019; 15: e1902136.

26. Deng M, Gui X, Kim J, Xie L, Chen W, Li Z, et al. LILRB4 signalling in leukaemia cells mediates T cell suppression and tumour infiltration. Nature. 2018; 562: 605-9.

27. Wu HL, Hu H, Wan JL, Li YM, Wu YX, Tang YX, et al. Hydroxyethyl starch stabilized polydopamine nanoparticles for cancer chemotherapy. Chem. Eng. J. 2018; 349: 129-45.

28. Xu J, Fang L, Shi M, Huang Y, Yao L, Zhao S, et al. A peptide-based four-color fluorescent polydopamine nanoprobe for multiplexed sensing and imaging of proteases in living cells. Chem Commun (Camb). 2019; 55: 1651-4.

29. Zhang M, Bai LL, Shang WH, Xie WJ, Ma H, Fu YY, et al. Facile synthesis of water-soluble, highly fluorescent graphenequantum dots as a robust biological label for stem cells. J Mater Chem. 2012; 22: 7461-7.

30. Mac QD, Mathews DV, Kahla JA, Stoffers CM, Delmas OM, Holt BA, et al. Non-invasive early detection of acute transplant rejection via nanosensors of granzyme B activity. Nat Biomed Eng. 2019; 3: 281-91.

31. MacCallum RM, Martin AC, Thornton JM. Antibody-antigen interactions: contact analysis and binding site topography. J Mol Biol. 1996; 262: 732-45.

32. Heidelberger M, Kendall FE. The Precipitin Reaction between Type Iii Pneumococcus Polysaccharide and Homologous Antibody: Iii. A Quantitative Study and a Theory of the Reaction Mechanism. J Exp Med. 1935; 61: 563-91.

33. Kang X, Kim J, Deng M, John S, Chen H, Wu G, et al. Inhibitory leukocyte immunoglobulin-like receptors: Immune checkpoint proteins and tumor sustaining factors. Cell Cycle. 2016; 15: 25-40.

34. Gui X, Deng M, Song H, Chen Y, Xie J, Li Z, et al. Disrupting LILRB4/APOE interaction by an efficacious humanized antibody reverses T-cell suppression and blocks AML development. Cancer Immunol. Res. 2019; 7: 1244-57.

35. Zhang R, Zhu Z, Lv H, Li F, Sun S, Li J, et al. Immune checkpoint blockade mediated by a small-molecule nanoinhibitor targeting the PD-1/PD-L1 pathway synergizes with photodynamic therapy to elicit antitumor immunity and antimetastatic effects on breast cancer. Small. 2019; 15: e1903881.

36. Xu X, Ho W, Zhang X, Bertrand N, Farokhzad O. Cancer nanomedicine: from targeted delivery to combination therapy. Trends Mol Med. 2015; 21: 223-32.

37. Suk JS, Xu Q, Kim N, Hanes J, Ensign LM. PEGylation as a strategy for improving nanoparticle-based drug and gene delivery. Adv Drug Deliv Rev. 2016; 99: 28-51.

38. Han X, Wang L, Li T, Zhang J, Zhang D, Li J, et al. Beyond Blocking: engineering RNAi-mediated targeted immune checkpoint nanoblocker enables T-cell-independent cancer treatment. ACS Nano. 2020, 14(12).

39. Philip M, Schietinger A. CD8(+) T cell differentiation and dysfunction in cancer. Nat. Rev. Immunol. 2022; 22: 209-23.

40. Postow MA, Sidlow R, Hellmann MD. Immune-related adverse events associated with immune checkpoint blockade. N. Engl. J. Med. 2018; 378: 158-68.

41. Ramos-Casals M, Brahmer JR, Callahan MK, Flores-Chavez A, Keegan N, Khamashta MA, et al. Immune-related adverse events of checkpoint inhibitors. Nat. Rev. Dis. Primers. 2020; 6: 38.

42. Larimer BM, Wehrenberg-Klee E, Dubois F, Mehta A, Kalomeris T, Flaherty K, et al. Granzyme B PET imaging as a predictive biomarker of immunotherapy response. Cancer Res. 2017; 77: 2318-27.

43. Ou YC, Wen X, Johnson CA, Shae D, Ayala OD, Webb JA, et al. Multimodal multiplexed immunoimaging with nanostars to detect multiple immunomarkers and monitor response to immunotherapies. ACS Nano. 2020; 14: 651-63.

44. Workman P, Aboagye EO, Balkwill F, Balmain A, Bruder G, Chaplin DJ, et al. Guidelines for the welfare and use of animals in cancer research. Br. J. Cancer. 2010; 102: 1555-77.

45. Anami Y, Deng M, Gui X, Yamaguchi A, Yamazaki CM, Zhang N, et al. LILRB4-targeting antibody-drug conjugates for the treatment of acute myeloid leukemia. Mol. Cancer Ther. 2020; 19: 2330-9.